ARTICLE IN PRESS

ELSEVIER

Available online at www.sciencedirect.com
SCIENCE DIRECT®

Journal of Petroleum Science and Engineering xx (2003) xxx–xxx

JOURNAL OF PETROLEUM SCIENCE & ENGINEERING

www.elsevier.com/locate/jpetscieng

Reconstruction of Berea sandstone and pore-scale modelling of wettability effects

Pål-Eric Øren*, Stig Bakke

Statoil Research Centre, N-7005 Trondheim, Norway

Received 29 July 2002; received in revised form 24 January 2003

Abstract

We present an integrated procedure for estimating permeability, conductivity, capillary pressure, and relative permeability of porous media. Although the method is general, we demonstrate its power and versatility on samples of Berea sandstone. The method utilizes petrographical information obtained from 2D thin sections to reconstruct 3D porous media. The permeability and conductivity are determined by solving numerically the local equations governing the transport. The reconstructed microstructure is transformed into a topologically equivalent network that is used directly as input to a network model. Computed two-phase and three-phase relative permeabilities for water wet conditions are in good agreement with experimental data. We present a method for characterizing wettability on the pore-scale from measured Amott wettability indices. Simulated effects of wettability on waterflood relative permeabilities and oil recovery compare favourably with experimental results.
© 2003 Elsevier Science B.V. All rights reserved.

Keywords: Berea; Wettability; Relative permeability; Oil recovery

1. Introduction

The microstructure of a porous medium and the physical characteristics of the solid and the fluids that occupy the pore space determine several macroscopic properties of the medium. These properties include petrophysical and transport properties of engineering interest, such as permeability, electrical conductivity, relaxation times, capillary pressure, and relative permeabilities. Understanding the relation between microstructure and physical properties is therefore of great theoretical and practical interest in many fields of technology. Important industrial examples arise in the production of oil and gas from petroleum bearing reservoirs and in pollutant transport and cleanup (Dullien, 1992).

The prediction of physical properties of porous media from their microscopic origins involves three major steps:

(i) A quantitative characterization of the microstructure.
(ii) Characterization of wettability and the relevant pore-scale physics.
(iii) Exact or approximate solutions of the equations of motion that govern the transport phenomena of interest.

Until the 1990s, attempts to relate physical properties of a rock to its microstructure were mainly

* Corresponding author.
E-mail address: peoe@statoil.com (P.-E. Øren).

0920-4105/03/$ - see front matter © 2003 Elsevier Science B.V. All rights reserved.
doi:10.1016/S0920-4105(03)00062-7

hampered by the difficulty of adequately describing the complex nature of the pore space. Direct measurements of a 3D microstructure are now available via synchrotron X-ray computed microtomography (Dunsmoir et al., 1991; Coles et al., 1994, 1996; Spanne et al., 1994; Hazlett, 1995; Coker et al., 1996). In practice, however, information about the microstructure of porous materials is often limited to 2D thin section images.

A number of *statistical* models have been proposed for reconstructing 3D porous media from 2D thin section images (Joshi, 1974; Quiblier, 1984; Adler et al., 1990, 1992; Adler, 1992; Roberts, 1997; Hazlett, 1997; Yeong and Torquato, 1998a,b; Manswart and Hilfer, 1998). In short, it consists of measuring statistical properties, such as porosity, correlation and lineal path functions on 2D thin section images of the sample. Random 3D models are then generated in such a manner that they match the measured statistical properties. Recent quantitative comparisons of these models with tomographic images of sedimentary rocks have shown that statistical reconstructions may differ significantly from the original sample in their geometric connectivity (Hazlett, 1997; Biswal et al., 1999; Manswart et al., 2000; Øren and Bakke, 2002).

In contrast to statistical models, *process-based* models try to account for the fact that the pore structure is often the result of physical processes. Bakke and Øren (1997) developed a process-based reconstruction procedure which incorporates grain size distribution and other petrographical data obtained from 2D thin sections to reconstruct 3D sandstones. Øren and Bakke (2002) applied the procedure to reconstruct Fontainebleau sandstone. Quantitative comparisons with microtomographic images showed that the reconstructed model adequately reproduced important geometrical and connectivity properties of the actual sandstone.

With the advance in computational fluid dynamics, it is now possible to compute single-phase properties such as permeability and conductivity directly on quite large 3D microstructure images (Adler et al., 1990, 1992; Schwartz et al., 1994; Ferreol and Rothman, 1995; Widjajakusuma et al., 1999; Øren and Bakke, 2002). This is generally not the case for multiphase flow. Although it is possible to solve the multiphase transport equations in pore spaces of arbitrary geometry (Rothman, 1990; Gunstensen and Rothman, 1993; Hazlett et al., 1998; Adler and Thovert, 1998), the solutions are computationally very expensive and in practice limited to relatively small 3D systems. A commonly applied simplification is to represent the microstructure by an interconnected network in which larger pores (pore bodies) are connected by smaller pores (throats). Since the pioneering work of Fatt (1956), network models have been used extensively to study different displacement processes in simple or idealized porous media.

The power and usefulness of network models are in their ability to relate macroscopic behaviour directly to the underlying pore-scale physics. Until the 1990s, most network model studies focused on two-phase flow phenomena. In recent years, our physical understanding of three-phase flow at the pore level has increased significantly (Kantzas et al., 1988; Øren and Pinczewski, 1992, 1995; Blunt et al., 1995; Keller et al., 1997). This has led to development of network models for three-phase flow (Øren et al., 1994; Pereira et al., 1996; Fenwick and Blunt, 1998a,b; Mani and Mohanty, 1998; Lerdahl et al., 2000). It is crucial, however, that network models are given proper pore structure information as input if they are to provide realistic predictions of transport properties.

Despite strong evidence that spatial correlations exist at the pore scale (Wardlaw et al., 1987; Bryant et al., 1993a,b; Knackstedt et al., 1998), most network models assume that the pore structure is random. There have been few attempts to construct pore networks that replicate the true microstructure of the medium. With the availability of tomographic or reconstructed 3D images, it is now possible to extract the exact network representation of the pore space and use it directly in network models. Sok et al. (2002) generated network replica of four tomographic images of Fontainebleau sandstone. Simulated two-phase flow properties were compared with those computed on equivalent stochastic networks. In all cases, the simulations on the stochastic networks provided a poor representation of the results from the direct network replica. Øren et al. (1998) reconstructed Bentheimer sandstone and extracted network replica of the microstructure. Predicted drainage and imbibition relative permeabilities for water wet conditions

were found to be in good agreement with experimental data.

The wettability characteristics of a reservoir rock plays a significant role in determining transport properties such as relative permeability, capillary pressure, and oil recovery. Predictive modelling of reservoir rocks thus requires an accurate characterization of wettability. Unfortunately, there is little experimental evidence of wettability and the appropriate fluid configurations on the pore scale in nonwater wet samples. Kovscek et al. (1993) proposed a theoretical pore level model for wettability alteration and fluid configurations that appears to capture much of the important physics of nonwater wet displacements. The model has been used to explore the effects of wettability on relative permeability and oil recovery (Dixit et al., 1999, 2000; Blunt, 1998; Øren et al., 1998). Dixit et al. (1998, 1999) introduced the regime theory that explained experimental trends in oil recovery in terms of wettability characterized by contact angles for the oil wet regions and the fraction of pores that become oil wet. Unfortunately, there is no a priori way of determining these parameters for reservoir rocks. The hope is that macroscopic measurements, such as Amott wettability indices, will be sufficient to estimate them.

In the present work, we reconstruct 3D Berea sandstone. To assess the quality of the reconstruction we compare quantitatively the geometry and the connectivity of the simulated microstructure with two other models of Berea sandstone. One of the models is a microtomographic image of the actual sandstone and the other one is a statistical reconstruction of the same rock. The permeability and formation factors of the models are derived by solving numerically the local equations governing the transport. Topological and geometrical analyses are then used to build network replica of the process-based reconstructed microstructure. Predicted two-phase and three-phase relative permeabilities for water wet conditions are compared with the experimental results of Oak (1990). Finally, we describe a physically based scenario for wettability alteration on the pore level and show how we can utilize measured Amott wettability indices to characterize wettability on the pore scale. We investigate how wettability affects waterflood relative permeabilities and oil recoveries. Computed oil recoveries for a range of wettability conditions are compared with the experimental results of Jadhunandan and Morrow (1995).

2. Reconstruction of Berea sandstone

2.1. Experimental sample

Berea sandstone has been used by the petroleum industry for many years as a standard material in core analysis research and in laboratory core flooding experiments. This is because the rock is relatively homogenous, well characterized and, until recently, readily available. It is made up of well-sorted and well-rounded predominately quartz grains, but it also contains minor amounts of feldspar, dolomite, and clays (Churcher et al., 1991).

The particular Berea sample that we study has a porosity of 23% and an absolute air permeability of 1100 mD (Hazlett, 1995). High resolution X-ray computer tomography was performed on a cylindrical microplug that was drilled from the larger original core. Details about the experimental apparatus and the image acquisition procedure are given by Jasti et al. (1993). Each voxel of this 3D image has a linear dimension of 10 μm and takes on the value 0 (solid and clays) or 1 (pore). The size of the reconstructed image is 128^3 voxels and the porosity $\phi_p = 0.1778$ which is to be compared with the experimental value of $\phi = 0.23$. The discrepancy in porosity is mainly attributed to the presence of clay microporosity below the 10-μm resolution of the thresholded image.

2.2. Process-based model

2.2.1. Thin section analysis

The input parameters for the process-based reconstruction algorithm are obtained from back-scattered electron (BSE) images of standard 2D petrographic thin sections. The BSE images are digitized and represented by an array of grey-scale values (0–255) according to the differences in atomic mass density. By appropriately thresholding the images, we can distinguish between different phases such as pore, quartz, clays, and feldspar. Proper thresholding is obtained by visual comparison of the original and thresholded images. Fig. 1 shows a BSE image of a thin section of Berea sandstone.

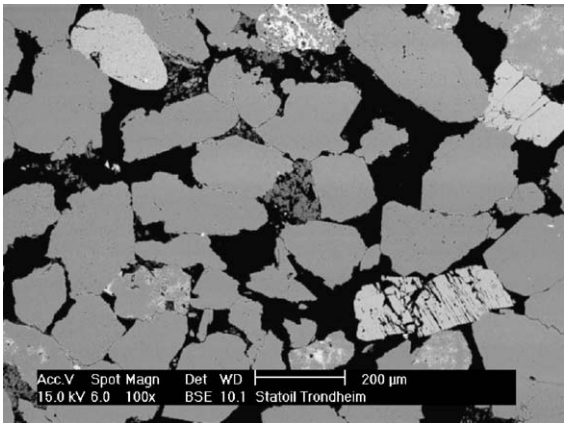

Fig. 1. BSE image of a thin section from Berea sandstone. The pore space is black, feldspar is light grey, quartz is medium grey, and clays are dark grey.

To describe each phase i in the image, we introduce the binary phase function

$$Z_i(\mathbf{x}) = \begin{cases} 1 & \text{if } \mathbf{x} \in \text{phase } i \\ 0 & \text{otherwise} \end{cases} \quad (1)$$

The intergranular porosity, ϕ_p, and the volume fraction of clays, ϕ_c, are calculated from Z as the statistical averages $\phi_p = \langle Z_p(\mathbf{x}) \rangle$ and $\phi_c = \langle Z_c(\mathbf{x}) \rangle$, respectively. For the images analysed here, $\phi_p \simeq 0.18$ and $\phi_c \simeq 0.09$. The clay texture was determined from visual observation and was found to be mainly pore filling kaolinite. The total porosity ϕ is calculated as $\phi = \phi_p + \phi_c \phi_{\mu c}$ where $\phi_{\mu c}$ is the microporosity of the clays which depends on the clay mineralogy and the clay texture.

An erosion–dilation algorithm is used to partition the solid matrix phase into discrete grains. We measure the minor diameter, d_1, and the major diameter, d_2, of each grain section by standard image analysis techniques. The size of the measured grains were in the range 80 μm $< d_1 <$ 330 μm. Most of the grains were well rounded and were assumed to be spherical (i.e. $d_1 \simeq d_2$). Approximately 20% of the grain sections were elliptical and the maximum aspect ratio, d_2/d_1, was equal to 1.6. We constructed a grain size distribution curve by numbering and sorting all the grains according to size. Approximately 1% of the grains were partially dissolved feldspars, the rest of the grains were quartz.

2.2.2. Sedimentation

Only spherical and ellipsoidal grains are considered. The grains are defined by their semiaxes ($r_1 \leq r_2 = r_3$), two of them being equal. Grains are picked randomly from the grain size distribution curve and dropped onto a predefined bounding box (grainbed) using a sequential deposition algorithm. The algorithm simulates the successive deposition of individual grains in a gravitational field. Each grain falls under the action of its own weight until it attains a stable position at a local or global minimum in potential energy. The sedimentation algorithm for spherical grains has been presented before (Bakke and Øren, 1997; Øren and Bakke, 2002).

The procedure for modelling ellipsoidal grains in a low-energy environment (local minimum) is as follows:

1. Randomly select a grain radius r_1 from the sorted grain size distribution curve.
2. Assign randomly an aspect ratio r_2/r_1 in the range $[1.0, (r_2/r_1)_{max}]$.
3. Increase the radii of all existing grains in the horizontal (x and y) and vertical directions by r_2 and r_1, respectively.
4. Drop the new grain (reduced to a point) onto the grainbed from a random location above the bed until it hits the bottom or the surface of the expanded grainbed.
5. Let the grain slide down steepest local gradient until it attains a stable position. If the surface of the top layer contains holes and the new grain rolls into one, the fall continues until the grain finds a stable position or it reaches the sides of the sample box.
6. Reset all the grain radii to their original values and repeat the above procedure for the next grain.

High-energy sedimentation is modelled by the same procedure by omitting steps 4 and 5 and simply placing each new grain at the lowest available position (i.e. global minimum) in the grainbed. Note that all the ellipsoidal grains are assumed to be arranged with their largest section horizontal.

2.2.3. Compaction and rearrangement

We model the results of compaction and rearrangement by shifting the vertical co-ordinate of every

grain centre towards the centre *xy*-plane of the model according to the formula

$$z = 0.5\lambda_z(z_{\max} - z_{\min}) + z_o(1 - \lambda_z + \epsilon_z) \quad (2)$$

where z is the new vertical position, z_o is the original one, λ_z is the compaction factor, and ϵ_z is a random variance that mimics grain rearrangement. Further details about the compaction modelling are given elsewhere (Bakke and Øren, 1997; Øren and Bakke, 2002). We modelled Berea sandstone using $\lambda_z = 0.05$ and ϵ_z randomly distributed in the interval $[-0.02, 0.02]$.

2.2.4. Diagenesis

Only a subset of known diagenetic processes are modelled, namely quartz cement overgrowth, dissolution and metasomatosis of feldspars, and authigenic clay growth. We model quartz cement overgrowth by an algorithm similar to that described by Schwartz and Kimminau (1987). If $R_o(r)$ denotes the radius of the originally deposited grain, its new radius along the direction r from the grain centre is given by

$$R(r) = R_o(r) + \min(\alpha l(r)^{\gamma}, l(r)) \quad (3)$$

where $l(r)$ is the distance between the surface of the original grain and the surface of its Voronoi polyhedron along the direction r. The constant α controls the amount of cement growth (i.e. the porosity). Positive values of α result in quartz cement growth while negative values mimic quartz dissolution or overpressured sandstones with abnormally large intergranular porosity.

The exponent γ controls the direction of cement growth. Positive values of γ favour growth of quartz cement in the directions of large $l(r)$ (i.e. pore bodies) while negative values favour growth of cement in the directions of small $l(r)$ (i.e. pore throats). If $\gamma = 0$, quartz cement grows equally in all directions as concentric overgrowth. The Berea sample was modelled using $\gamma = 0.5$.

Pore lining clays such as chlorite typically form crystals that grow radially outward from the surface of the detrital grains. We model such clays by randomly precipitating clay particles on the surfaces of the grains or the quartz cement. Pore filling clays such as pseudo-hexagonal booklets of kaolinite are modelled using a clustering algorithm which causes new clay particles to precipitate preferentially in randomly selected pore bodies that already contain clay. The modelling of pore bridging clays, such as illite, is more complex and we refer the interested reader to Øren and Bakke (2002). For the Berea sample, the volume fraction of clay ϕ_c was 0.09. Approximately 90% of the clays were deposited as pore filling while the rest was precipitated as pore lining.

Dissolution of feldspars may result in a variety of secondary porosity textures. Feldspar may be partially or completely dissolved and replaced by either void or microporous clay. The dissolution pattern sometimes reflects the crystal structure of the feldspar while clay may show feldspar pseudomorphism. For the Berea sample, we model these processes by randomly converting 20% of the feldspar grains into microporous clay and 10% into void. The main input parameters for the reconstruction of Berea sandstone are summarized in Table 1.

2.2.5. Gridding

For practical purposes, we construct the medium in a discrete manner. The reconstruction is performed on a 3D grid of size $M_x \times M_y \times M_z$ with lattice spacing a. The discretized medium is composed of small cubes, each of size a, that are filled either with void or with solid. The solid cubes or voxels are characterized in terms of their mineralogy (quartz, feldspar, or clay). The Berea sandstone was con-

Table 1
Input parameters for the process based reconstruction of Berea sandstone

ϕ_p	0.18	intergranular porosity
ϕ_c	0.09	volume fraction of clays
ϕ_f	0.01	volume fraction of feldspar
d_1	80–330 μm	grain diameter
f_{ell}	0.20	fraction ellipsoidal grains
d_2/d_1	[1, 1.6]	grain aspect ratio
λ_z	0.05	compaction factor
ϵ_z	[−0.02, 0.02]	compaction variance
γ	0.5	quartz cement exponent
$p-f$	0.90	fraction pore filling clays
$p-l$	0.10	fraction pore lining clays

structed on a cubic grid of size 300^3 voxels. The lattice constant $a = 10$ μm.

2.3. Statistical model

We follow the reconstruction algorithm proposed by Yeong and Torquato (1998b) for reconstruction of a two-phase porous medium. The main idea is to generate a 3D configuration that matches certain stochastic functions of a reference medium. In our case, the reference medium is the microtomography image. The reconstruction is carried out in a discrete manner by use of a simulated annealing algorithm (Kirkpatrick et al., 1983). The target or energy function is defined as

$$E_t = \sum_{k=1}^{J} \omega_k \sum_{\mathbf{x}} \left| f_t^k(\mathbf{x}) - f_{\mathrm{ref}}^k(\mathbf{x}) \right|^2 \tag{4}$$

where f_{ref}^k is the kth function of a set of J stochastic functions to be reconstructed, f_t^k is the value of this function at iteration step t, and ω_k is the weight of the kth function.

Starting from a random configuration with porosity ϕ_{p}, two voxels of different phases (i.e. matrix and pore) are chosen randomly and swapped. The porosity is thus preserved during the reconstruction process. The new energy is computed according to Eq. (4) and the new configuration is accepted with probability

$$p = \begin{cases} 1 & \text{if } \Delta E \leq 0 \\ e^{-\Delta E/T} & \text{if } \Delta E > 0 \end{cases} \tag{5}$$

where $\Delta E = E_t - E_{t-1}$ and T is a fictitious temperature. If the swap is rejected, the old configuration is restored. By decreasing the temperature, the system evolves gradually towards a configuration which minimizes the "energy".

The temperature is reduced if the total number of iterations, at each temperature, exceeds MT. These MT iterations represent one Markov chain. The new temperature is computed as

$$T_m = T_0 \exp[(\lambda - 1)m] \tag{6}$$

where T_m is new temperature for the mth Markov chain. The starting temperature T_0 was estimated by setting the initial acceptance rate to 0.5. We use a constant reduction factor $\lambda = 0.9$ and an optimal Markov chain length $MT = 200$ (Ouenes et al., 1994). The process terminates when $E_t < 10^{-5}$ or after a certain number of consecutive rejections.

2.3.1. Reconstructed functions

The microstructure of a two-phase medium that consists of a pore phase and a matrix phase (solid and clays) is described in detail by the phase function $Z(\mathbf{x})$

$$Z(\mathbf{x}) = \begin{cases} 1 & \text{if } \mathbf{x} \in \text{pore space} \\ 0 & \text{otherwise} \end{cases} \tag{7}$$

The porosity is the statistical average $\phi_{\mathrm{p}} = \langle Z(\mathbf{x}) \rangle$ while the two-point correlation function $G_2(\mathbf{u})$ is defined as

$$G_2(\mathbf{u}) = \frac{\langle (Z(\mathbf{x}) - \phi_{\mathrm{p}})(Z(\mathbf{x}+\mathbf{u}) - \phi_{\mathrm{p}}) \rangle}{\phi_{\mathrm{p}}(1 - \phi_{\mathrm{p}})} \tag{8}$$

For a discretized medium, the position vector $\mathbf{x}$ and the translation vector $\mathbf{u}$ only take discrete values. If the medium is homogenous and isotropic, $G_2(\mathbf{u}) = G_2(\|\mathbf{u}\|) = G_2(u)$. In this case, it is sufficient to sample G_2 only in the directions of the principal axis. Hence, G_2 is calculated for every pair of voxels by successively translating a line of length $u = 0, 1, \ldots, u_{\mathrm{c}}$ voxels along the three orthogonal directions of the sample.

The lineal path function $PL(u)$ is defined as the probability of finding a line segment of length u entirely in the pore space. Hence, $PL(0) = \phi_{\mathrm{p}}$ holds. $PL(u)$ is evaluated for each pore voxel in all three orthogonal directions by counting the number $l(u)$ of segments that fall entirely in the pore space

$$PL(u) = \frac{l(u)}{m} \tag{9}$$

where m is the total number of placements of the segment of length u. We use a cut-off length $u_c = 50$ voxels for both G_2 and PL and impose periodic boundary conditions on the sample boundaries. During the reconstruction, we update only those terms of G_2 and PL that have been affected by the exchange of voxels. This was accomplished by storage of line-by-line contributions of the functions. Both functions had the same weight $\omega_1 = \omega_2 = 0.5$.

3. Reconstructed Berea models

Fig. 2 shows the 3D pore space in a 128^3 voxels subregion of the different Berea models. The micro-tomographic image is denoted CT, the process-based model PM and the statistical model SM. Visual inspection suggests that none of the reconstructed microstructures closely resemble that of the micro-tomography image. This is especially the case for sample SM which appears to be more tortuous. Visually, the process-based reconstruction provides a better representation of the true sandstone microstructure. However, it is important to realize that average properties of different media may agree closely even if visual appearances suggest otherwise.

3.1. Local porosity distributions

Local porosity distributions (Hilfer, 1991, 1996) are obtained from the indicator $Z(\mathbf{x})$ in the following way: Let $\phi(\mathbf{x}, L) = \langle Z(\mathbf{x}) \rangle_{\mathcal{M}}$ denote the porosity of a

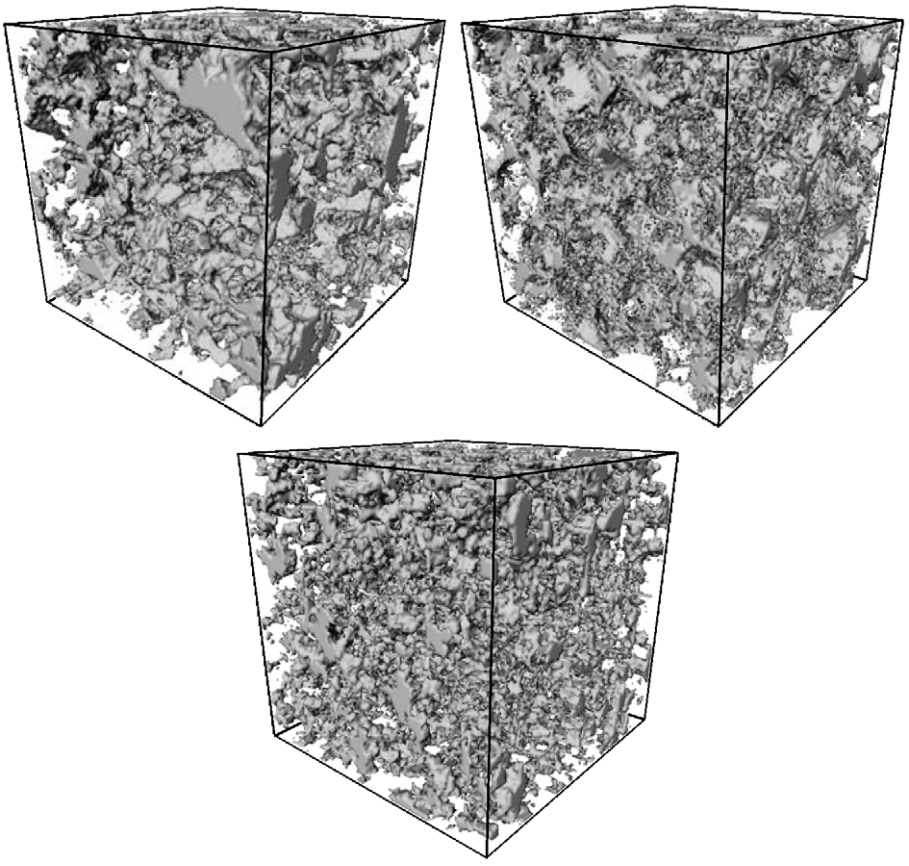

Fig. 2. The pore space in a 128^3 voxels subregion of samples CT (left), PM (right), and SM (bottom). The resolution of all the images is 10 μm.

cubic measurement cell $\mathcal{M}(\mathbf{x}, L)$ of side length L centred at position $\mathbf{x}$. The local porosity distribution, $\mu(\phi, L)$ is then defined as

$$\mu(\phi, L) = \frac{1}{m} \sum_{\mathbf{x}} \delta(\phi - \phi(\mathbf{x}, L)) \tag{10}$$

with the indicator

$$\delta(\phi - \phi(\mathbf{x}, L)) = \begin{cases} 1 & \text{if } |\phi - \phi(\mathbf{x}, L)| \leq \Delta\phi \\ 0 & \text{otherwise} \end{cases} \tag{11}$$

$\mu(\phi, L)$ is the probability density that a given measurement cell of side length L has a porosity in the range $[\phi, \phi \pm \Delta\phi]$. In Eq. (10), m denotes the total number of measurement cells. Ideally, the measurement cells should not overlap, but in practice this cannot be done because of poor statistics (Biswal et al., 1998, 1999). The present results were obtained by placing $\mathcal{M}(\mathbf{x}, L)$ on all voxels which are at least a distance $L/2$ from the boundaries of the sample.

The local porosity distributions $\mu(\phi, L^*)$ of the three samples are shown in Fig. 3. The characteristic length $L^* = 150$ μm. Although differences do exist, the local porosity distributions of the three models are fairly similar. Unfortunately, characterization of the samples in terms of $\mu(\phi, L^*)$ does not allow us to quantify the connectivity of the samples. Transport properties, of course, depend critically on the connectivity of the pore space.

3.2. Fraction percolating cells

A measurement cell $\mathcal{M}$ is said to percolate in all three directions if each face in the cell is connected to the opposite face by a continuous path that lies entirely inside the pore space. The total fraction of percolating cells, $P(L)$, is given by

$$P(L) = \frac{1}{m} \sum_{\mathbf{x}} \Lambda(\mathbf{x}, L) \tag{12}$$

where $\Lambda(\mathbf{x}, L)$ is an indicator of percolation

$$\Lambda(\mathbf{x}, L) = \begin{cases} 1 & \text{if } \mathcal{M}(\mathbf{x}, L) \text{ percolates} \\ 0 & \text{otherwise} \end{cases} \tag{13}$$

$P(L)$ is the probability of finding a measurement cell of side length L that percolates in all three directions and it is thus a measure of the geometrical connectivity of the medium.

Fig. 3 shows the total fraction of cells that percolates in all three directions as a function of L for the three samples. The connectivities of samples CT and PM are quite similar. This indicates that the process-based reconstruction is able to reproduce the intrinsic 3D connectivity properties of the actual sandstone.

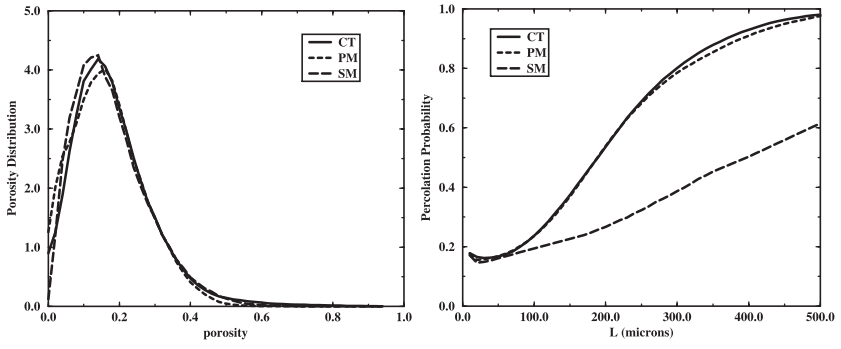

Fig. 3. Local porosity distributions $\mu(\phi, 150)$ for samples SM, CT, and PM (left). Fraction percolating cells versus L for the three samples (right).

This does not appear to be the case for the statistical reconstruction. Sample SM shows a drastically reduced connectivity compared to the other samples particularly at large L.

3.3. Transport properties

3.3.1. Formation factor

The directional formation factor, F_i, is defined as the inverse of the macroscopic electrical conductivity, σ_i, of a porous medium in a given i direction:

$$F_i = \frac{\sigma_w}{\sigma_i}, \tag{14}$$

where σ_w is the bulk electrical conductivity of the fluid that fills the pore space. We compute σ_i for the three orthogonal directions from a linear relation between the total electrical flux, Q_i, and the applied potential gradient, $(\Phi_I - \Phi_O)/L$:

$$Q_i = -\sigma_i \frac{\Phi_I - \Phi_O}{L} A \tag{15}$$

The potential Φ_I is applied to an inlet face, Ω_I, of area A, and the potential Φ_O to an outlet face, Ω_O, separated from Ω_I by a distance L. To obtain the electrical flux, we solve the Laplace equation

$$\nabla(\sigma_w \nabla \Phi) = 0 \tag{16}$$

subject to the boundary condition

$$\nabla \Phi \cdot \mathbf{n} = 0 \quad \text{on } S_p \tag{17}$$

where $\mathbf{n}$ is the unit vector normal to the pore wall S_p. The microscopic fluid conductivity σ_w is given by

$$\sigma_w(x,y,z) = \begin{cases} 1 & \text{if } (x,y,z) \text{ is inside the pore} \\ 0 & \text{otherwise} \end{cases} \tag{18}$$

The electrical field is calculated from Φ by $\mathbf{E} = -\sigma_i \nabla \Phi$, and the total electrical flux through Ω_I is

$$Q_i = \int_{\Omega_I} \mathbf{n}\mathbf{E} \mathrm{d}\Omega_I \tag{19}$$

Details of the solution strategy are described by Øren and Bakke (2002). The average formation factor is defined as the harmonic mean of the directional dependent formation factors, i.e.,

$$\frac{1}{F} = \frac{1}{3}\left(\frac{1}{F_x} + \frac{1}{F_y} + \frac{1}{F_z}\right) \tag{20}$$

3.3.2. Permeability

The directional dependent absolute permeability, k_i, is defined by Darcy's law

$$Q_i = \frac{k_i}{\mu} \frac{(p_I - p_O)}{L} A \tag{21}$$

where Q_i is the macroscopic flux obtained from applying a macroscopic pressure gradient $(p_I - p_O)/L$ in a direction i. The low Reynolds number flow of an incompressible Newtonian fluid is governed by the usual Stokes equations

$$\mu \nabla^2 v = \nabla p \tag{22}$$

$$\nabla v = 0 \tag{23}$$

$$v = 0 \text{ on } S_p \tag{24}$$

where v, p, and μ are the velocity, pressure, and fluid viscosity, respectively. We employ the artificial compressibility scheme (Peyret and Taylor, 1983) to solve this partial differential equation on the digitized samples. From the resulting velocity field, the macroscopic flux Q_i is obtained by integrating v over the inlet area. A directionally averaged permeability is defined as the arithmetic mean $k = (k_x + k_y + k_z)/3$.

The computed transport properties for the different samples are summarized in Table 2. As expected, sample SM has a significantly lower conductivity and permeability than sample CT. This shows that the pore space of the statistical reconstruction is significantly more tortuous and less connected than that of the microtomography data. The directionally averaged formation factor of the process-based reconstruction is similar to that of sample CT (36.9 versus 41.6) while the permeability is roughly 20% higher.

Table 2
Computed transport properties for the samples (experimental sample denoted EX)

Property	CT	PM	SM	EX
F_x	40.4	33.1	81.9	
F_y	38.5	36.3	78.8	
F_z	46.8	42.6	103.0	
F	41.6	36.9	86.9	
k_x (mD)	861	1040	243	
k_y (mD)	891	965	254	
k_z (mD)	622	822	167	
k (mD)	791	942	221	1100

In general, we find the agreement between samples PM and CT quite encouraging.

4. Network representation

4.1. Topology

The topology or connectivity of the reconstructed medium is characterized by the skeleton which can be viewed as a line representation of the pore space, analogous to a capillary network. The skeleton of sandstones that contain microporosity and secondary porosity can be very complex. To simplify matters, we extract the skeleton from the intergranular pore space that is defined by the sedimentary grains and the quartz cement.

We do this by an ultimate dilation of the grains (Bakke and Øren, 1997). The vertices of the resulting Voronoi polyhedra are defined by the voxels that have neighbouring voxels from four or more different grains and can be viewed as the nodes of the network. The edges of the polyhedra consist of voxels that have neighbouring voxels from three different grains and define the flow paths (links) between the nodes.

Many characteristic network model parameters can be obtained directly from the skeleton provided that some care is exercised. In particular, dead ends must be removed and certain nodes must be fused into a single node. In general, neighbouring nodes are fused into a single node if their inscribed sphere radii overlap. After the fusing operations, the remaining nodes and links are in a one-to-one correspondence with the percolating pore bodies and throats of the intergranular pore space.

The co-ordination number of a node is the number of links connected to it. This is an important connectivity characteristic that can be obtained directly from the skeleton. Fig. 4 shows the distribution of measured co-ordination numbers. The co-ordination number ranges from 1 to 16 with an average value of 4.45. This is in agreement with values for Berea sandstone reported in the literature (Jerauld and Salter, 1990).

4.2. Pore body and throat sizes

The nodes (vertices) of the skeleton are used to determine the pore body sizes. Briefly, for each

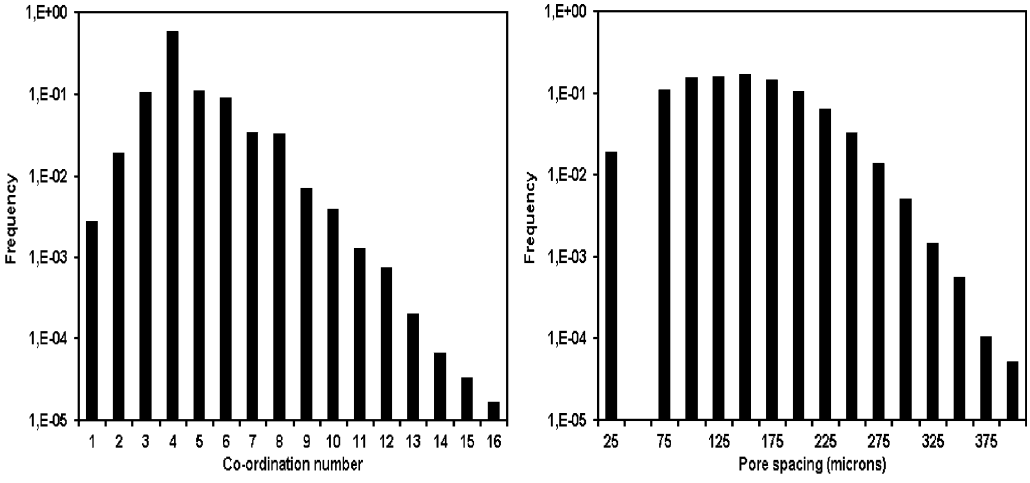

Fig. 4. Measured distributions of (left) co-ordination numbers and (right) channel lengths for the process-based reconstruction of Berea.

node, the pore walls are mapped using a rotating radius vector in a plane that is centred on the node voxel. This plane is rotated 18 times in increments of 10° and all the distances from the node voxel to the quartz/clay surfaces are recorded. Abnormally long distances are assumed to have been measured into pore throats and are neglected. The highest distance transform voxel next to the node defines the radius of an inscribed sphere. We define this radius as the size of the pore body. Fig. 5 shows the distribution of pore body sizes. The average pore body size is 27 μm.

Pore throat sizes are measured similarly. For each skeleton voxel, the pore walls between two connecting nodes are mapped in a plane that is perpendicular to the local direction of the throat. The throat radius in each plane is measured using a radius vector that is rotated 36 times in increments of 10°. The inscribed radius for each plane is recorded. The smallest radius corresponds to the throat constriction and it is defined as the effective size of the pore throat. Fig. 5 shows the measured distribution of throat sizes for the reconstructed Berea. The average throat size is 14 μm.

The cross-sectional shape of every pore body and throat is described in terms of a dimensionless shape factor $G=A/P^2$ where A and P are the average area and perimeter length, respectively, of the planes used in the mapping of the pore body or throat. The shape factor approximates the irregular shape of a pore body or throat by an equivalent irregular triangular, cubic, or cylindrical shape (Øren et al., 1998). Fig. 6 shows the distribution of shape factors for the pore bodies and throats.

4.3. Lengths and volumes

We define the pore channel length, l_{ij}, as the length between two connecting nodes i and j on the skeleton. The distribution of channel lengths for the reconstructed Berea is shown in Fig. 4. For network modelling purposes, we also define an effective pore body length l_i and an effective throat length l_t according to

$$l_i = l_i^t\left(1 - 0.5\frac{r_t}{r_i}\right) \tag{25}$$

$$l_j = l_j^t\left(1 - 0.5\frac{r_t}{r_j}\right) \tag{26}$$

$$l_t = l_{ij} - l_i - l_j \tag{27}$$

where $l^t_{i(j)}$ is the distance between node $i(j)$ and the channel constriction, r_t, is the radius at the constriction, and $r_{i(j)}$ is the radius of pore body $i(j)$. The intergranular volume of each pore body, V_p, is deter-

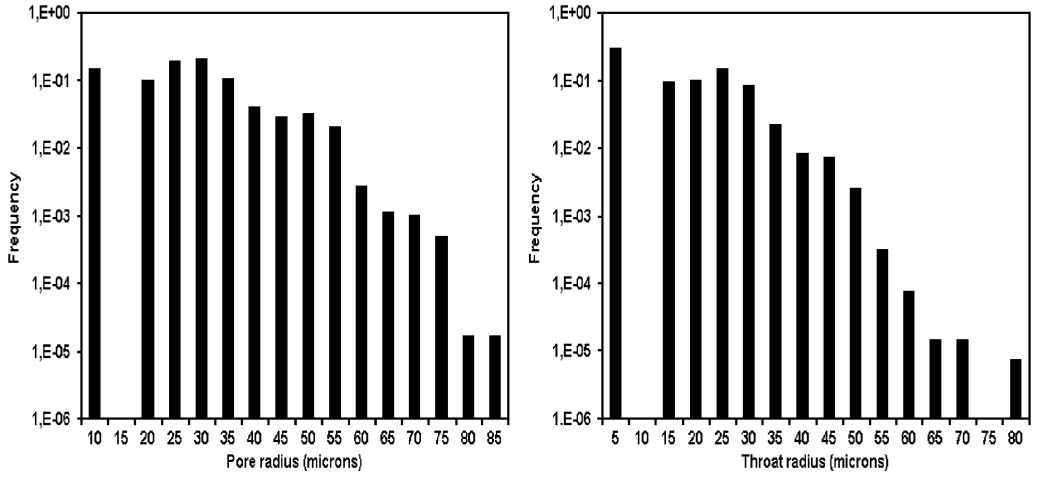

Fig. 5. Measured pore body (left) and throat (right) size distributions for the reconstructed Berea.

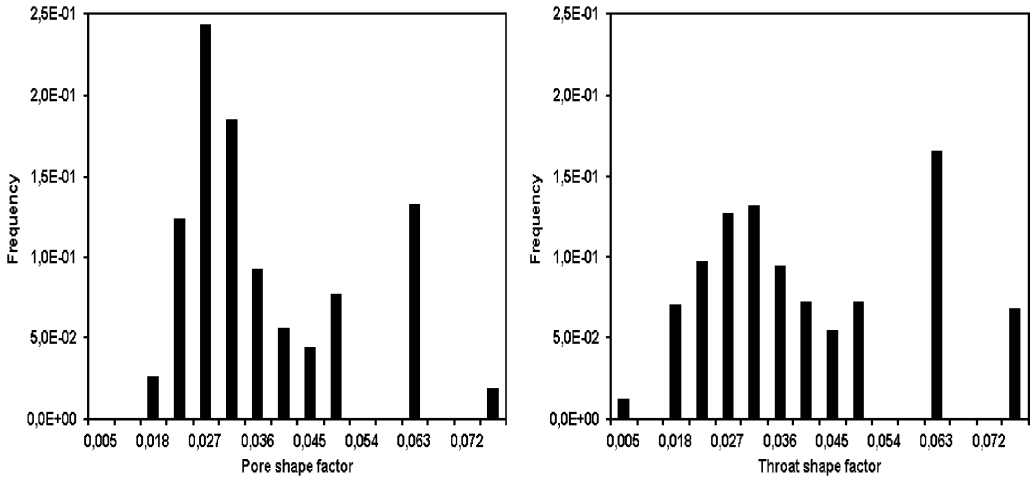

Fig. 6. Measured distributions of pore and throat shape factors.

mined by measuring the volume out to each of the connecting throats. Similarly, the intergranular volume of each throat, V_t, is measured by counting the number of pore voxels inside the domain bounded by planes located at l_i and l_j. We note that l_i and l_j, and hence V_t, depend on the pore body-to-throat aspect ratio (i.e. $r_{i(j)}/r_t$) and that V_t decreases as the aspect ratio increases. The clay associated volume V_c of every pore body or throat is determined by counting the number of clay voxels inside the pore body or throat domain. The total pore volume of the model is given as

$$PV = \sum_{i=1}^{\text{ntot}} (V_{p,i} + \phi_{\mu c} V_{c,i}) + \sum_{l=1}^{\text{ltot}} (V_{t,l} + \phi_{\mu c} V_{c,l}) \quad (28)$$

where ntot and ltot are the total number of pore bodies and throats, respectively, and $\phi_{\mu c}$ is the clay porosity. We model the porous clay as a bundle of parallel pores with fractal cross section. The fractal model is constructed by an iterative process which commences by dividing the half perimeter of a circular pore of radius r_0 in n parts and replacing each part by half a circle (Vizika and Lenormand, 1991). The radius $r_0 = 1/2a\phi_{\mu c}$ where a is the resolution of the reconstructed model. The linear fractal dimension is taken to be $D_L = 1.6$, which is typical of sandstones.

5. Effects of wettability

The predictive power of network modelling techniques for strongly water wet systems is well established (Bryant and Blunt, 1992; Bakke and Øren, 1997; Øren et al., 1998; Lerdahl et al., 2000). However, few, if any, oil reservoirs are strongly water wet. Predictive modelling of reservoir rocks thus requires an accurate characterization of wettability. Below, we describe what has recently become the standard model for describing wettability effects in network models. Although the model has not been validated through quantitative predictions for non-water wet rocks, it appears to capture much of the pertinent physics.

Kovscek et al. (1993) proposed a physically based pore level scenario of wettability change and fluid distribution. Initially, we consider the reservoir rock to be fully saturated with water and strongly water wet. When oil invades the pore space during oil migration, a water film protects the pore surface from being contacted by oil. The stability of the water film depends on the prevailing capillary pressure and on the shape of the disjoining pressure isotherm. At a critical capillary pressure, the water film ruptures, oil contacts the pore surface, and its wettability changes. Regions of the pore space where the thick water film coats the pore surface remain water wet as do the water-filled corners of oil invaded pores, as shown in Fig. 7a. The

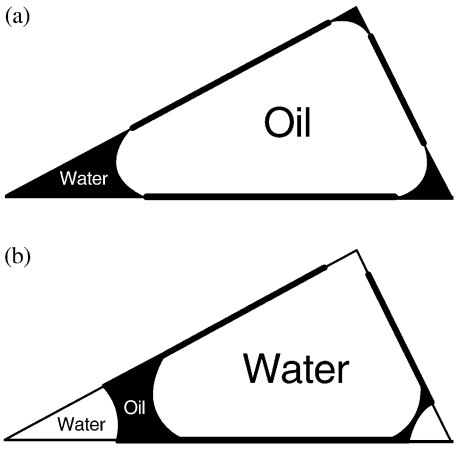

Fig. 7. (a) Oil and water in a triangular pore or throat after primary drainage. The areas contacted by oil have altered wettability while the water-filled corners remain water wet. (b) Formation of oil films in the corners during waterflooding.

degree of wettability alteration depends on the composition of the oil and brine and on the mineralogy of the pore surface.

Within a single pore, different parts of the pore surface have different wettability. The corners are water wet while the centre of the pore is oil wet. This results in a number of different fluid configurations during waterflooding. If the bulk portion of a pore is oil wet, water invades the pore as a nonwetting phase and resides in the centre of the pore. In this case, a film of oil may be sandwiched in between the water in the corner and the water in the centre, as shown in Fig. 7b. These films may significantly increase the connectivity of the oil and allow oil mobility down to low oil saturations.

Kovscek et al. (1993) examined the different fluid configurations of this wettability model in pores with a grain boundary shape. Blunt (1997) extended the analysis to square pores while Øren et al. (1998) and Patzek (2001) examined the fluid configurations in triangular pores and provided mathematical details of entry capillary pressures. Using this pore level scenario for wettability change, the effects of wettability on relative permeability and oil recovery have been explored (Blunt, 1998; Dixit et al., 1999, 2000; Øren et al., 1998).

The key parameters in this mixed wettability model are the fraction α_1 of oil-invaded pores that become oil wet, the spatial distribution of the oil wet pores, and the contact angles. In the presence of contact angle hysteresis, the advancing contact angle θ_a is greater than the receding angle θ_r. Consequently, some of the pores that are oil wet during waterflooding ($\theta_a > 90°$) will be water wet during secondary drainage ($\theta_r < 90°$). We thus need to estimate the fraction α_2 that are oil wet during secondary drainage. Unfortunately, there is no a priori way of determining these parameters. The hope is that macroscopic measurements, such as Amott wettability indices, would be sufficient to estimate the parameters and allow quantitative predictions for nonwater wet samples. Recently, Dixit et al. (2000) derived limiting analytical relationships between Amott wettability indices and α_1 for a bundle of capillary tubes. Here we attempt to extend their analysis by including accessibility effects, phase trapping and contact angle hysteresis.

5.1. Amott wettability indices

The Amott test is one of the most widely used empirical wettability measurements for reservoir cores. The method combines two spontaneous imbibition measurements and two forced displacement measurements (see Fig. 8). The Amott water index $I_w = \Delta S_1/(\Delta S_1 + \Delta S_2)$, where ΔS_1 is the change in

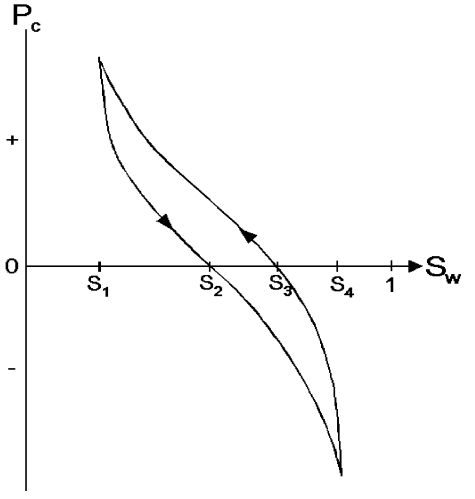

Fig. 8. Schematic definition of the Amott indices to water (I_w) and oil (I_o) in terms of capillary pressure curves. $I_w = (S_2 - S_1)/(S_4 - S_1)$, $I_o = (S_4 - S_3)/(S_4 - S_1)$.

water saturation due to spontaneous imbibition and ΔS_2 is the additional change in water saturation due to forced displacement. Similarly, the Amott oil index $I_o = \Delta S_3/(\Delta S_3 + \Delta S_4)$. The two indices are often combined to give the Amott–Harvey index $I_{wo} = I_w - I_o$. I_{wo} varies between $+1$ (strongly water wet) and -1 (strongly oil wet).

Consider first the process of spontaneous water imbibition. If the water saturation at the start of the imbibition is S_{wi}, the saturation change due to water imbibition can be expressed as

$$\Delta S_1 = (1 - S_{wi} - S_{ow1})a_1 \tag{29}$$

where S_{ow1} is the volume fraction of oil wet pores ($\theta_a > 90°$) and a_1 is a trapping function for the water wet regions defined as

$$a_1 = 1 - \frac{S_{or,ww}}{1 - S_{wi} - S_{ow1}} \tag{30}$$

where $S_{or,ww}$ is the residual oil saturation in water wet pores. The volume fraction of oil wet pores $S_{ow1} = \alpha_1 f_{s1}$ where f_{s1} is a saturation conversion function that depends on the distribution of the oil wet pores. If the oil wet pores are randomly distributed, wettability is uncorrelated with pore size and $f_{s1} = 1 - S_{wi}$. If wettability is correlated with pore size, f_{s1} depends on the pore size distribution.

Similarly, the additional change in water saturation due to forced displacement can be expressed as

$$\Delta S_2 = \alpha_1 f_{s1} a_2 \tag{31}$$

where a_2 is a trapping function for the oil wet regions defined as

$$a_2 = 1 - \frac{S_{or,ow1}}{S_{ow1}} \tag{32}$$

where $S_{or,ow1}$ is the residual oil saturation in the oil wet pores.

By combining Eqs. (29) and (31), the fraction of oil wet pores can be expressed in terms of I_w as

$$\alpha_1 = \frac{1 - S_{wi}}{f_{s1}} \left[1 + \frac{a_2}{a_1} \left(\frac{I_w}{1 - I_w} \right) \right]^{-1} \tag{33}$$

If there is no contact angle hysteresis, pores that are oil wet during waterflooding are also oil wet during secondary drainage (i.e. $\alpha_1 = \alpha_2$). In a more realistic scenario, θ_r is different from θ_a and $\alpha_2 < \alpha_1$. This is always true for mixed wet systems where θ_r may be much less than θ_a. The change in water saturation due to spontaneous oil imbibition can be expressed as

$$\Delta S_3 = S_{ow2} a_3 = \alpha_2 f_{s2} a_3 \tag{34}$$

where the accessibility function a_3 is given by

$$a_3 = 1 - \left(\frac{S_{or,ow2} + S^{imb}_{w,ow2}}{S_{ow2}} \right) \tag{35}$$

where $S_{or,ow2}$ is the residual oil saturation in oil wet pores ($\theta_r > 90°$) at the end of the forced water displacement and $S^{imb}_{w,ow2}$ is the volume fraction of oil wet pores that are filled with water at the end of the oil imbibition. Furthermore, if we assume that there is little or no water trapping during secondary drainage, the change in water saturation due to oil imbibition can be written as

$$\Delta S_3 \simeq \Delta S_2 \frac{I_o}{1 - I_w} \tag{36}$$

By combining Eqs. (31), (34), and (36), the fraction of oil wet pores during secondary drainage is given by

$$\alpha_2 = \alpha_1 \frac{f_{s1} a_2}{f_{s2} a_3} \frac{I_o}{1 - I_w} \tag{37}$$

We note that if θ_a for the oil wet pores are randomly distributed between some upper and lower values, f_{s2} equals f_{s1} evaluated at α_1.

5.2. Trapping and accessibility functions

To determine α_1 from a given I_w, we need to estimate the three functions a_1, a_2, and f_{s1}. As mentioned before, f_{s1} depends on the particular distribution of oil wet pores. We shall consider three possible distributions: (i) oil wet pore bodies are randomly distributed, denoted MWR, (ii) the largest pore bodies preferentially become oil wet, denoted

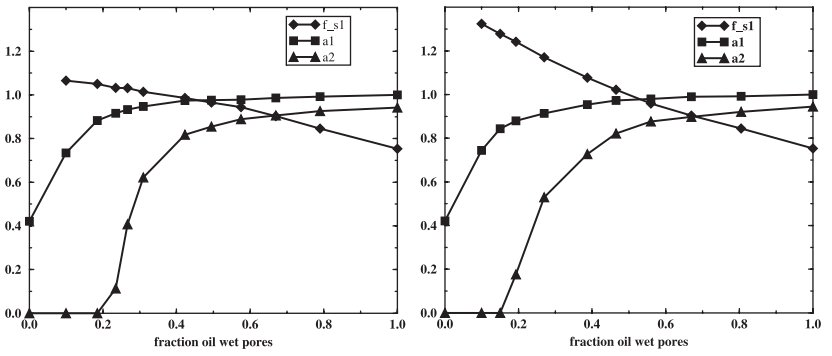

Fig. 9. The functions a_1, a_2, and f_{s1} for MWL (left) and MWC (right) versus α_1. The initial water saturation $S_{wi}=0.25$.

MWL, and (iii) clay-rich pore bodies preferentially become oil wet, denoted MWC. For all three distributions we assume that the throat contact angle is correlated to the contact angles in the two connecting pore bodies.

In Fig. 9, simulated values of the three functions are plotted versus α_1 for the MWL and MWC cases. The results for MWR were similar. In all the simulations, θ_a was distributed randomly between 20° and 90° for the water wet pores and 90° and 160° for the oil wet pores. The saturation function, f_{s1}, varies almost linearly with α_1 for the MWL and MWC cases. We also note that $f_{s1}^{MWL}>f_{s1}^{MWC}>f_{s1}^{MWR}=1-S_{wi}$.

The oil wet trapping function a_2 is zero until α_1 reaches a critical value α_{1c}. For $\alpha_1<\alpha_{1c}$, no spanning oil wet cluster exist and oil can only be displaced at positive capillary pressures (i.e. $I_w=1$). If $\alpha_1>\alpha_{1c}$, spanning oil wet clusters exist and oil can be displaced from oil wet pores by forced displacement. The exact value of α_{1c} depends on the distribution of oil wet pores. For the Berea sample considered here, $\alpha_{1c}(S_{wi}=0.25)=0.15$, 0.19, and 0.25 for the MWL, MWC, and MWR, respectively. For $\alpha_1>\alpha_{1c}$, the water wet trapping function a_1 is fairly close to 1. Since we are mainly interested in cases where $\alpha_1>\alpha_{1c}$ (i.e. $I_w<1$), we make the simplification that $a_1\simeq 1$.

The trapping function a_2 is mainly determined by the collapse of oil films in the corners of oil wet pores. This in turn depends on details such as the corner half angle, the contact angle, and the maximum capillary pressure reached during primary drainage (i.e. S_{wi}) (Øren et al., 1998). It is therefore almost impossible to a priori predict a_2 for realistic cases. To come up with an approximate expression for a_2, we performed a number of waterflood simulations commencing at different S_{wi}. The computed $(1-a_2)$ values show a strong power law behaviour when plotted versus S_{ow1c}/S_{ow1} (Fig. 10) where S_{ow1c} is the volume fraction of oil wet pores at α_{1c}. We propose to estimate a_2 by the following empirical expression

$$a_2 = 1 - 1.2\left(\frac{S_{ow1c}}{S_{ow1}}\right)^{2.1} \tag{38}$$

The simulated accessibility function a_3 is plotted versus α_2 in Fig. 11. It is similar for the MWL, MWC,

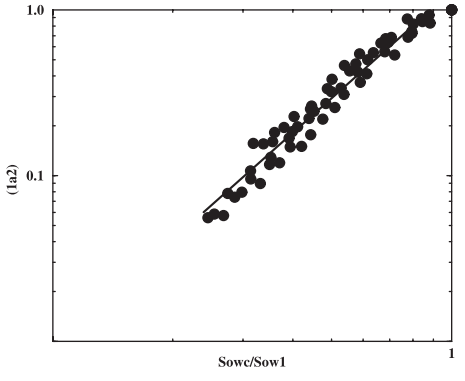

Fig. 10. Scaling of the oil wet trapping function a_2. In the simulations, the initial water saturation was varied between 0.25 and 0.4.

and MWR cases and increases rapidly towards an asymptotic value for $\alpha_2 > \alpha_{2c}$. The asymptotic value is $1 - S^*_{or}$ where S^*_{or} is the residual oil saturation for the strongly oil wet case ($\alpha_2 = 1$). For a given rock-fluid system, S^*_{or} depends principally on S_{wi} and decreases as S_{wi} is reduced. For low S_{wi}, the initial capillary pressure is larger than for high S_{wi}. This improves the stability of the oil films and allows more oil to be recovered by film drainage. Similar to a_2, we observe a strong power law behaviour when we plot $(1 - a_3)$ versus S_{ow2c}/S_{ow2} (Fig. 11) and we propose the following empirical expression

$$a_3 = 1 - \left(\frac{S_{ow2c}}{S_{ow2}}\right)^{2Z} \tag{39}$$

where Z is the average co-ordination number of the pore network.

5.3. Contact angle hysteresis

It is well known that the effective advancing angle during waterflooding is always higher than the effective receding angle during drainage. This apparent hysteresis is due to pore surface roughness, adsorption of surface active materials, and pore geometry effects (i.e. diverging/converging geometries). Morrow and McCaffery (1975) measured advancing and receding angles of many chemicals in air/liquid/teflon systems. With sufficient roughening of the Teflon core, they obtained fairly consistent results that were independent of pore size and further roughening. Their results (referred to as Class III) are shown in Fig. 12 where the advancing and receding angles are plotted versus the equilibrium angle θ_e measured on a at surface.

It is of course unclear how these results for low-energy solids can be used to predict the wetting behaviour of porous media formed from high-energy solids such as quartz. Since many crude oil/brine/rock systems are known to display high contact angle hysteresis (Buckley, 1993), we suspect that the predicted hysteresis may be too small. However, in the absence of direct information, we will assume that contact angle hysteresis in our Berea sample can be described by the Class III type.

Since θ_a and θ_r can be characterized in terms of θ_e, the problem of distributing advancing and receding angles is reduced to determine the distribution of equilibrium contact angles. We define θ_{e1} to be the equilibrium angle corresponding to $\theta_a = 90°$ and θ_{e2} to be the equilibrium angle at which $\theta_r = 90°$. Unless the sample is strongly water wet ($I_w = 1$), we simply assume θ_e for the water wet pores to be randomly distributed in the range $[20° - \theta_{e1}]$.

Similarly, for the oil wet pores, we assume that θ_e is randomly distributed in the range $[\theta_{e,min} < \theta_e < \theta_{e,max}]$ where $\theta_{e,min} = \theta_{e1}$ and $\theta_{e,max}$ depends on α_2 and is given by

$$\theta_{e,max} = \theta_{e2} + \frac{\alpha_2}{1 - \alpha_2}(\theta_{e2} - \theta_{e,min}). \tag{40}$$

We note that $\theta_{e,max}$ increases as the system becomes more strongly oil wet. For large values of α_2, $\theta_{e,max}$ determined from Eq. (40) may be larger than 180°.

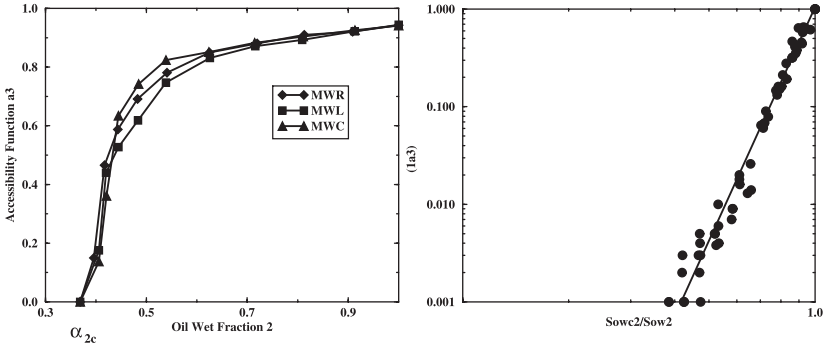

Fig. 11. (left) Simulated values of the accessibility function a_3 versus α_2 for $S_{wi} = 0.25$. (right) Power law behaviour of a_3.

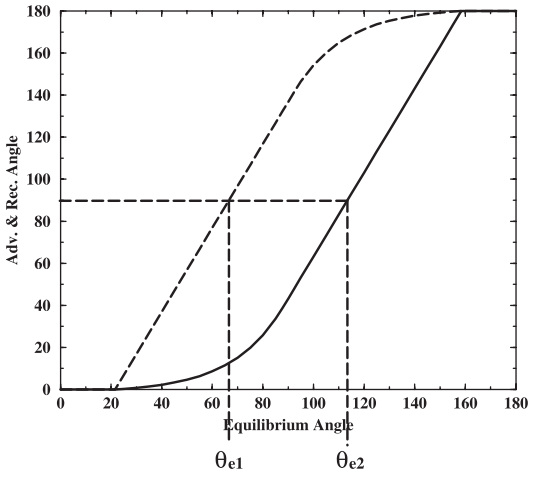

Fig. 12. Effect of surface roughness on advancing and receding contact angles.

In this case, $\theta_{e,max}=180^\circ$ and we adjust $\theta_{e,min}$ according to

$$\theta_{e,min} = \theta_{e2} - \frac{1-\alpha_2}{\alpha_2}(180^\circ - \theta_{e2}) \quad (41)$$

We note that the proposed method for distributing contact angles is general and not model specific, as long as θ_a and θ_r can be characterized in terms of θ_e.

6. Results and discussion

A detailed description of the network simulator used to simulate two-phase and three-phase displacements in our reconstructed networks can be found in Øren et al. (1998), Lerdahl et al. (2000), and Patzek (2001). Since these papers provide a clear and comprehensive discussion of all the mathematical details, we will not repeat them here.

6.1. Water wet results

Fig. 13 shows measured and predicted two-phase relative permeabilities for water wet Berea. The experimental data are steady-state measurements taken from Oak (1990). To predict the primary drainage relative permeability, the receding contact angle was everywhere assumed to be 0. Oak (1990) observed that the gas–liquid imbibition relative permeability was different than the oil–water imbibition relative permeability, suggesting that the gas was a more strongly nonwetting phase than oil. For waterflooding, even in water wet sandstones using refined oils, the advancing contact angle is typically at least 30°–60° (Dullien, 1992). This apparent contact angle hysteresis is due to pore surface roughness and converging/diverging pore geometries. For the waterflood, we assumed that the contact angle was randomly distributed in the range 20°–50° while for the gas–liquid imbibition the contact angle was randomly distributed between 10° and 30°, consistent with a strongly water wet system. The predicted relative permeabilites shown in Fig. 13 are in good agreement with the experimental results.

Fig. 14 compares measured and predicted three-phase relative permeabilities for tertiary gas flooding in water wet Berea. The gas, water, and oil relative permeabilities all compare favourably with the experimental results. The simulated water and gas relative permeabilities were largely insensitive to the saturation history while the oil relative permeability depended strongly on the saturation history as evidenced by the scatter in both the simulated and experimental data. Further discussion of the three-phase results are given by Lerdahl et al. (2000). The agreement between simulated and measured relative permeabilities clearly illustrate the predictive power of our approach, at least for water wet systems.

6.2. Mixed wet results

We will first examine if we can reproduce target Amott water and oil indices using the procedure described in the previous section. Simulated I_w values are plotted versus target I_w in Fig. 15. There is good agreement between input and output I_w values for both the $S_{wi}=0.25$ and $S_{wi}=0.35$ cases. I_o was assumed to be 0 in these simulations. Simulated I_o values are also plotted versus input I_o in Fig. 15. Again, there is good agreement for both the MWR, MWL, and MWC cases. Although we may be able to reproduce measured Amott water and oil indices, predictive modelling of wettability effects may still be a long way off since there is no direct way of verifying that our characterization of wettability is an accurate representation of the actual wettability. We can only hope that

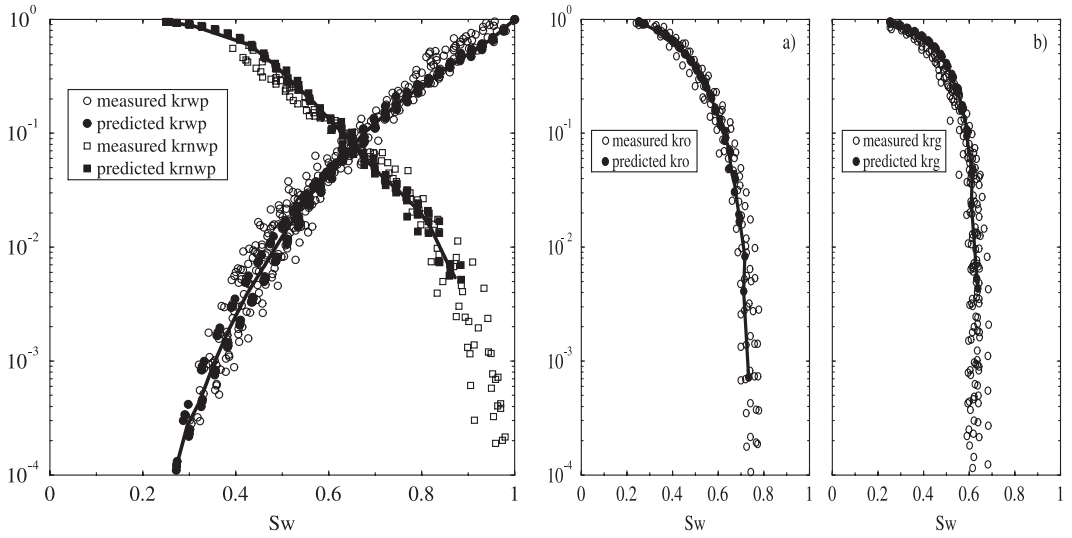

Fig. 13. Predicted versus measured relative permeabilities: (left) primary drainage, and (right) oil water imbibition (a) and gas–liquid imbibition (b).

the characterization is sufficient to capture most of the pertinent effects that wettability has on macroscopic properties such as relative permeability and oil recovery.

Jadhunandan and Morrow (1995) examined the effects of wettability on oil recovery in Berea sandstone using Moutray and ST-86 crude oil. The effects of brine composition, ageing temperature, and initial water saturation on wettability alteration were thoroughly studied. They observed a strong correlation between I_{wo} and S_{wi} with low S_{wi} values yielding the most oil wet cores. Furthermore, they found that waterflood oil recovery initially increased and then decreased as the wettability changed from strongly water wet to oil wet. Maximum oil recovery was obtained at very weak water wet conditions (small, but positive I_{wo}). This qualitative trend in recovery has been demonstrated previously in network model

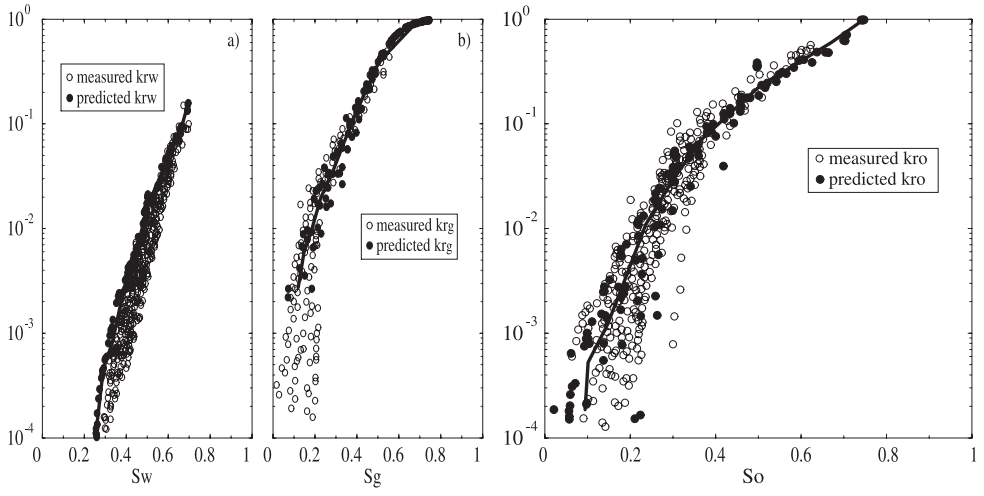

Fig. 14. Comparisons between predicted and measured three-phase gas, oil, and water relative permeabilities. The three-phase displacements commenced at different initial oil saturations.

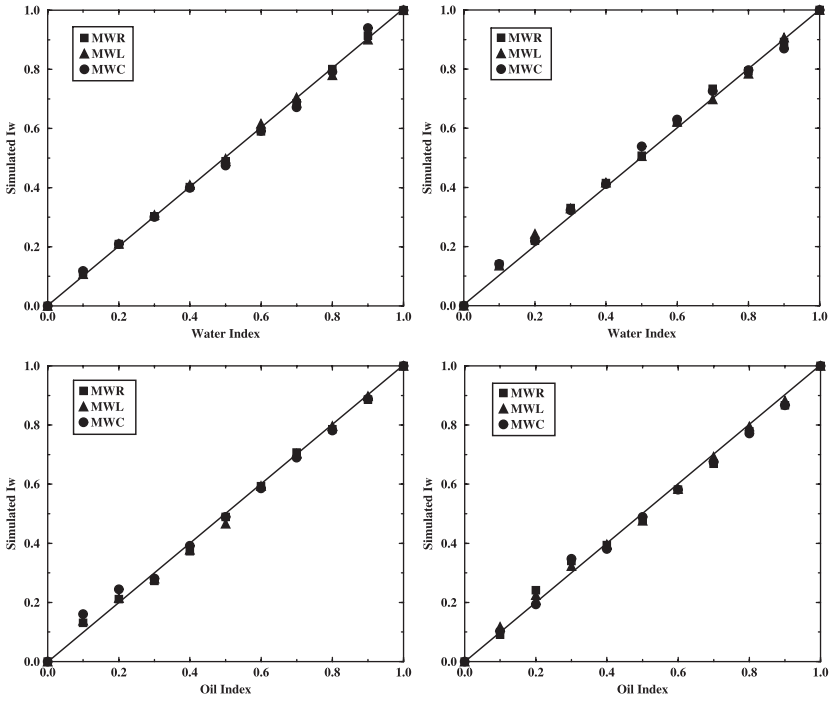

Fig. 15. Simulated Amott water and oil indices versus input indices: (top) water index and (bottom) oil index. The plots to the left are for $S_{wi}=0.25$ and the plots to the right for $S_{wi}=0.35$.

studies (Blunt, 1998; Dixit et al., 1999, 2000). There are two main differences in the present work. First, we attempt a quantitative match with experiments. Second, earlier the trend has been modelled by keeping S_{wi} constant and changing the fraction of oil wet pores. In the present study, I_{wo} and thus the fraction of oil wet pores vary with S_{wi}.

Using the experimentally observed correlation between I_{wo} and S_{wi}, we computed a number of waterflood relative permeability curves for different I_{wo}. Buckley–Leverett analysis were performed using the simulated relative permeability curves. In Fig. 16, the computed oil recovery efficiencies and the corresponding residual oil saturations after 3 and 20 pore volumes of water have been injected are plotted versus I_{wo}. The maximum oil recovery takes place at weak water wet conditions in complete agreement with the experimental results.

The pore-scale explanation for the results is as follows. For large I_{wo} (high S_{wi}), the waterflood advances principally by imbibition mechanisms. Because of the high S_{wi}, the oil phase is easily trapped in water wet pores that prevent oil film drainage. As S_{wi} (and I_{wo}) decreases, the waterflood advances by a combination of imbibition and drainage mechanisms. This leads to a more connected advance and reduced oil trapping in water wet pores. This gives a delayed water breakthrough and improved oil recovery. For low values of S_{wi} ($I_{wo}<0$), the waterflood is basically a drainage displacement and water preferentially fills the larger pores. This increases the water relative permeability and results in early breakthrough and reduced oil recovery. Recovery continues after breakthrough by film drainage, but this is a very slow process.

Quantitatively, the simulated oil recoveries (and residual oil saturations) agree fairly well with the measured data, although we seem to underpredict the maximum oil recovery. The discrepancy between simulated and observed maximum oil recovery is probably a result of too small contact angle hysteresis (i.e. θ_a is too small). As mentioned before, many crude oil/brine/rock systems display high contact

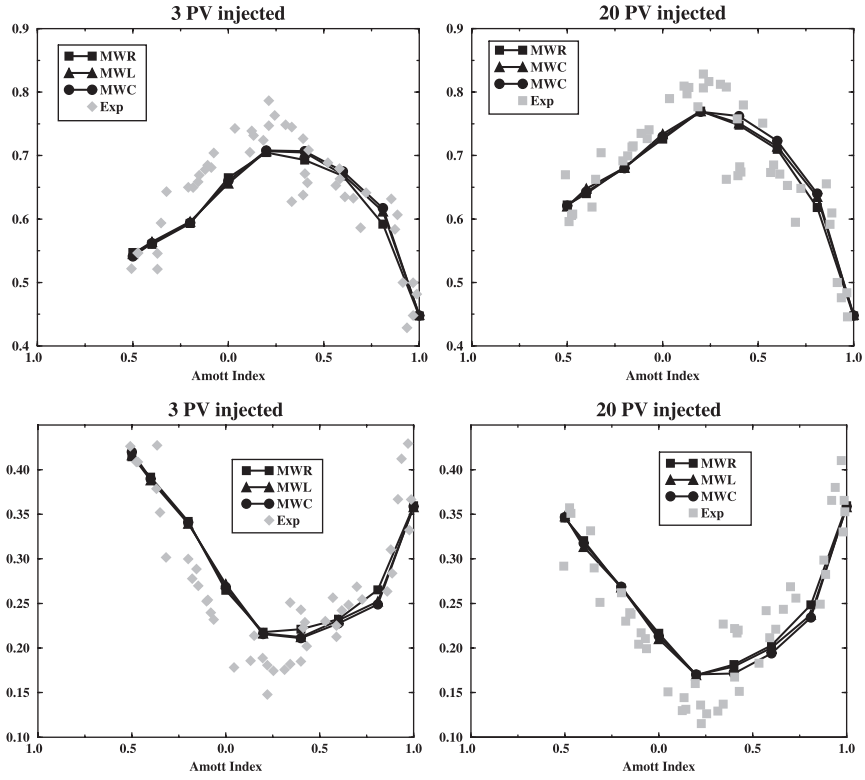

Fig. 16. Simulated and experimentally measured oil recovery efficiencies (top) and the corresponding residual oil saturations (bottom) versus I_{wo}.

angle hysteresis. If θ_a increases, the oil film in the corners of oil wet pores is stable over a larger range of capillary pressure and more oil can be recovered by film drainage.

The computed oil recoveries are fairly insensitive to the way that the oil wet pores are distributed. This suggests that it is more important to accurately determine the fraction of oil wet pores than the exact spatial distribution of these pores. This is in agreement with the results of McDougall and Sorbie (1995). Using a regular cubic network, they investigated how oil recovery varied with the fraction of oil wet pores. Both for the MWR and MWL cases, they found that maximum oil recovery occurred at $\alpha_1 \simeq 0.5$. The qualitative features of the two recovery curves were also similar. For $I_{wo} < 0$, the MWR, MWL, and MWC results are almost identical. This is because almost all the oil invaded pores are oil wet ($\alpha_1 \simeq 1$) and because the contact angles are distributed randomly.

7. Conclusions

We have presented a process-based method for reconstructing 3D sandstones from information that can be obtained from readily available 2D thin section images. By modelling the results of different sandstone forming processes, a wide range of unconsolidated and consolidated sandstones can be generated. We specifically applied the method to reconstruct Berea sandstone.

A quantitative comparison between the experimental microstructure of a Berea sandstone and a reconstructed model shows that intrinsic properties, such as porosity distributions and connectivity, are adequately captured in the reconstruction. Computed conductivities and permeabilities for the samples are in good agreement.

The reconstructed microstructure has been transformed into a topologically equivalent network that

was used directly as input to a network model. The network model accurately predicted both two-phase and three-phase relative permeabilities of water wet Berea.

We have presented a physically based model for wettability alterations on the pore scale and proposed a method for estimating the key parameters of this model from measured Amott oil and water indices. Using a published model for contact angle hysteresis, we are able to reproduce measured Amott wettability indices and examine how waterflood oil recovery varies with wettability. The simulated oil recoveries initially increased and then decreased as the wettability became more oil wet. Maximum oil recovery occurred at weak water wet conditions, in complete agreement with experimental evidence.

The present results clearly show the predictive power of our procedure, at least for water wet systems. However, predictive modelling of reservoir rocks that are nonwater wet may still be a long way off. Although we may be able to reproduce measured Amott indices, there is no direct evidence that our characterization of wettability on the pore scale is accurate. Much more work is needed before the proposed methodology can be used with confidence in the modelling of diverse reservoir rocks. It is also unclear how accurately we can reconstruct the microstructure of more heterogeneous and diagentically complex rocks such as those often encountered in the oil industry.

Acknowledgements

The authors acknowledge Den Norske Stats Oljeselskap (Statoil) for granting permission to publish this paper. We thank Dr. Randy Hazlett for providing the X-ray microtomography data.

References

Adler, P.M., 1992. Porous Media: Geometry and Transports. Butterworth/Heineman, Stoneham.

Adler, P.M., Thovert, J.F., 1998. Real porous media: local geometry and macroscopic properties. Applied Mechanics Reviews 51, 537–585.

Adler, P.M., Jacquin, C.G., Quiblier, J.A., 1990. Flow in simulated porous media. International Journal of Multiphase Flow 16, 691–712.

Adler, P.M., Jacquin, C.G., Thovert, J.F., 1992. The formation factor of reconstructed porous media. Water Resources Research 28, 1571–1576.

Bakke, S., Øren, P.E., 1997. 3-D pore-scale modelling of sandstones and flow simulations in the pore networks. SPE Journal 2, 136–149.

Biswal, B., Manwarth, C., Hilfer, R., 1998. Three-dimensional local porosity analysis of porous media. Physica. A 255, 221–241.

Biswal, B., Manswarth, C., Hilfer, R., Bakke, S., Øren, P.E., 1999. Quantitative analysis of experimental and synthetic microstructures for sedimentary rocks. Physica. A 273, 452–475.

Blunt, M., 1997. Pore level modelling of the effects of wettability. SPE Journal 2, 494–510.

Blunt, M., 1998. Physically-based network modeling of multiphase flow in intermediate–wet porous media. Journal of Petroleum Science and Engineering 20, 117–125.

Blunt, M., Zhou, D., Fenwick, D., 1995. Three-phase flow and gravity drainage in porous media. Transport in Porous Media 20, 77–103.

Bryant, S.L., Blunt, M., 1992. Prediction of relative permeability in simple porous media. Physical Review. A 46, 2004–2111.

Bryant, S.L., King, P.R., Mellor, D.W., 1993a. Network model evaluation of permeability and spatial correlation in a real random sphere packing. Transport in Porous Media 11, 53–70.

Bryant, S.L., Cade, C.A., Mellor, D.W., 1993b. Permeability prediction from geological models. AAPG Bulletin 77, 1338–1350.

Buckley, J.S., 1993. Mechanisms and consequences of wettability alterations by crude oils. PhD thesis, Heriot-Watt University, 1996.

Churcher, P.L., French, P.R., Shaw, J.C., Schramm, L.L., 1991. Rock properties of Berea sandstone, Baker dolomite, and Indiane limestone, paper SPE 21044. Proceedings of the 1991 SPE International Symposium on Oilfield Chemistry, Anaheim, Feb. 20–22.

Coker, D.A., Torquato, S., Dunsmoir, J.H., 1996. Morphology and physical properties of Fontainebleau sandstone via tomographic analysis. Journal of Geophysical Research 101, 497–506.

Coles, M.E., Spanne, P., Muegge, E.L., Jones, K.W., 1994. Computer microtomography of reservoir core samples. Proceedings of the 1994 Annual SCA Meeting, Stavanger, Norway, Sept. 12–14.

Coles, M.E., Hazlett, R.D., Muegge, E.L., Jones, K.W., Andrews, B., Siddons, P., Peskin, A., Soll, W.E., 1996. Developments in synchroton X-ray microtomography with applications to flow in porous media, paper SPE 36531. Proceedings of the 1996 SPE Annual Technical Conference and Exhibition, Denver, Oct. 6–9.

Dixit, A.B., McDougall, S.R., Sorbie, K.S., 1998. Analysis of relative permeability hysteresis trends in mixed wet porous media using network models, paper SPE 39656. Proceedings of the SPE/DOE Improved Oil Recovery Symposium, Tulsa, April 19–22.

Dixit, A.B., McDougall, S.R., Sorbie, K.S., Buckley, J.S., 1999.

Pore-scale modeling of wettability effects and their influence on oil recovery. SPERE 2, 25–36.

Dixit, A.B., Buckley, J.S., McDougall, S.R., Sorbie, K.S., 2000. Empirical measures of wettability in porous media and the relationship between them derived from pore-scale modeling. Transport in Porous Media 40, 27–54.

Dullien, F.A.L., 1992. Porous Media: Fluid Transport and Pore Structure, 2nd ed. Academic Press, New York.

Dunsmoir, J.H., Ferguson, S.R., D'Amico, K.L., Stokes, J.P., 1991. X-ray microtomography: a new tool for the characterization of porous media, paper SPE 22860. Proceedings of the 1991 SPE Annual Technical Conference and Exhibition, Dallas, Oct. 6–9.

Fatt, I., 1956. The network model of porous media: I. Capillary pressure characteristics. Transactions of AIME 207, 144–159.

Fenwick, D., Blunt, M., 1998a. Network modelling of three-phase flow in porous media. SPE Journal 3, 86–97.

Fenwick, D., Blunt, M., 1998b. Three-dimensional modelling of three-phase imbibition and drainage. Advances in Water Resources 25, 121–143.

Ferreol, B., Rothman, D.H., 1995. Lattice–Boltzmann simulations of flow through Fontainebleau sandstone. Transport in Porous Media 20, 3–20.

Gunstensen, A.K., Rothman, D.H., 1993. Lattice–Boltsmann studies of two-phase flow through porous media. Journal of Geophysical Research 98, 6431–6441.

Hazlett, R.D., 1995. Simulation of capillary dominated displacements in microtomographic images of reservoir rocks. Transport in Porous Media 20, 21–35.

Hazlett, R.D., 1997. Statistical characterization and stochastic modelling of pore networks in relation to fluid flow. Mathematical Geology 29, 801–822.

Hazlett, R.D., Chen, S.Y., Soll, W.E., 1998. Wettability and rate effects on immiscible displacement: Lattice Boltzmann simulation in microtomographic images of reservoir rocks. Journal of Petroleum Science and Engineering 20, 167–175.

Hilfer, R., 1991. Geometric and dielectric characterization of porous media. Physical Review. B, 60–75.

Hilfer, R., 1996. Transport and relaxation phenomena in porous media. Advances in Chemical Physics XCII, 299–424.

Jadhunandan, P.P., Morrow, N.R., 1995. Effect of wettability on waterflood recovery for crude-oil/brine/rock systems. SPE Reservoir Engineering 10, 40–46.

Jasti, J.K., Jesion, G., Feldkamp, L., 1993. Microscopic imaging of porous media with X-ray computer tomography. SPE Reservoir Engineering 8, 189–193.

Jerauld, G.R., Salter, S.J., 1990. The effect of pore-structure on hysteresis in relative permeability and capillary pressure: pore-level modelling. SPE Transport in Porous Media 5, 103–151.

Joshi, M., 1974. A class of stochastic models for porous media. PhD thesis, University of Kansas.

Kantzas, A., Chatziz, I., Dullien, F.A.L., 1988. Enhanced oil recovery by inert gas injection, paper SPE 13264. Proceedings of the Sixth SPE/DOE Symposium on Enhanced Oil Recovery, Tulsa, USA.

Keller, A.A., Blunt, M., Roberts, P.V., 1997. Micromodel observations of the role of oil layers in three-phase flow. Transport in Porous Media 26, 277–297.

Kirkpatrick, S., Gelatt, C.D., Vechi, M.P., 1983. Optimization by simulated annealing. Science 220, 671.

Knackstedt, M.A., Sheppard, A.P., Pinczewski, W.V., 1998. Simulation of mercury porosimetry on correlated grids: evidence of extended correlated heterogeneity at the pore scale in rocks. Physical Review. E, Rapid Communications 58, R6923–R6926.

Kovscek, A.R., Wong, H., Radke, C.J., 1993. A pore-level scenario for the development of mixed wettability in oil reservoirs. AIChE Journal 39, 1072–1085.

Lerdahl, T.R., Øren, P.E., Bakke, S., 2000. A predictive network model for three-phase flow in porous media, paper SPE 59311. Proceedings of the SPE/DOE Symposium on Enhanced Oil Recovery, Tulsa, April 3–5.

Mani, V., Mohanty, K.K., 1998. Pore-level network modelling of three-phase capillary pressure and relative permeability curves. SPE Journal 3, 238–248.

Manswart, C., Hilfer, R., 1998. Reconstruction of random media using Monte Carlo methods. Physical Review. E 59, 5596–5599.

Manswart, C., Torquato, S., Hilfer, R., 2000. Stochastic reconstruction of sandstones. Physical Review. E 62, 893–899.

McDougall, S.R., Sorbie, K.S., 1995. The impact of wettability on waterflooding: pore-scale simulation. SPE Reservoir Engineering August, 208–213.

Morrow, N.R., McCaffery, F.G., 1975. Displacement studies in uniformly wetted porous media. Journal of Canadian Petroleum Technology 15, 49.

Oak, M.J., 1990. Three-phase relative permeability of water wet Berea, paper SPE 20183. Proceedings of the SPE/DOE Symposium on Enhanced Oil Recovery, Tulsa, USA.

Øren, P.E., Bakke, S., 2002. Process based reconstruction of sandstones and predictions of transport properties. Transport in Porous Media 46, 311–343.

Øren, P.E., Pinczewski, W.V., 1992. Mobilization of waterflood residual oil by gas injection for water wet systems. SPE Formation Evaluation 7, 70–78.

Øren, P.E., Pinczewski, W.V., 1995. Fluid distribution and pore-scale displacement mechanisms in drainage dominated three-phase flow. Transport in Porous Media 20, 105–133.

Øren, P.E., Billiotte, J., Pinczewski, W.V., 1994. Pore-scale network modelling of waterflood residual oil recovery by immiscible gas flooding, paper SPE 27814. Proceedings of the Ninth SPE/DOE Symposium on Enhanced Oil Recovery, Tulsa, April 17–20.

Øren, P.E., Bakke, S., Arntzen, O.J., 1998. Extending predictive capabilities to network models. SPE Journal 3, 324–336.

Ouenes, A., Bhagavan, S., Bunge, P.H., Travis, B.J., 1994. Application of simulated annealing and other global optimization methods to reservoir description: myths and realities, paper SPE 28415. Proceedings of the 69th SPE Annual Technical Conference and Exhibition, New Orleans, September 25–28.

Patzek, T.W., 2001. Verification of a complete pore network simulator of drainage and imbibition. SPE Journal 6, 144–156.

Pereira, G.G., Pinczewski, W.V., Chan, D.Y.C., Paterson, L., Øren, P.E., 1996. Pore-scale network model for drainage dominated three-phase flow in porous media. Transport in Porous Media 24, 167–201.

ARTICLE IN PRESS

Peyret, R., Taylor, T.D., 1983. Computational Methods for Fluid Flow. Springer-Verlag, New York.

Quiblier, J.A., 1984. A new three-dimensional modelling technique for studying porous media. Journal of Colloid and Interface Science 98, 84–102.

Roberts, A.P., 1997. Statistical reconstruction of three-dimensional porous media from two-dimensional images. Physical Review. E 56, 3203–3212.

Rothman, D.H., 1990. Macroscopic laws for immiscible two-phase flow in porous media: results from numerical experiments. Journal of Geophysical Research 95, 8663.

Schwartz, L.M., Kimminau, S., 1987. Analysis of electrical conduction in the grain consolidation model. Geophysics 52, 1402–1411.

Schwartz, L.M., Auzerais, F., Dunsmoir, J.H., Marys, N., Bentz, D.P., Torquato, S., 1994. Transport and diffusion in three-dimensional composite media. Physica. A 207, 28–36.

Sok, R.M., Knackstedt, M.A., Sheppard, A.P., Pinczewski, W.V., Lindquist, W.B., Venkatarangan, A., Paterson, L., 2002. Direct and stochastic generation of network models from tomographic images: effect of topology on two phase flow properties. Transport in Porous Media 46, 345–372.

Spanne, P., Thovert, J.F., Jacquin, C.J., Lindquist, W.B., Jones, K.W., Adler, P.M., 1994. Synchrotron computed microtomography of porous media: topology and transports. Physical Review Letters 73, 2001–2004.

Vizika, O., Lenormand, R., 1991. Flow by film of the wetting phase in a porous medium and its role on the gravity drainage process. Proceedings of the IEA 12th International Workshop and Symposium, Bath, UK, October 28–30.

Wardlaw, N.C., Li, Y., Forbes, D., 1987. Pore-throat size correlation from capillary pressure curves. Transport in Porous Media 2, 597–614.

Widjajakusuma, J., Manswart, C., Biswal, B., Hilfer, R., 1999. Exact and approximate calculations for the conductivity of sandstones. Physica. A 270, 325–331.

Yeong, C.L.Y., Torquato, S., 1998a. Reconstructing random media. Physical Review. E 57, 495–506.

Yeong, C.L.Y., Torquato, S., 1998b. Reconstructing random media: II. Three-dimensional media from two-dimensional cuts. Physical Review. E 58, 224–233.